be examined in a similar light before they can be unambiguously interpreted to constrain the absolute chronology of late Pleistocene sea level and ice volume change.

References and Notes

1. J. Imbrie *et al.*, in *Milankovitch and Climate, Part 1*, A. L. Berger, J. Imbrie, J. Hays, G. Kukla, B. Saltzman, Eds. (Reidel, Dordrecht, Netherlands, 1984), pp. 269–305.
2. B. M. Hickey, *Prog. Oceanogr.* **8**, 191 (1979).
3. W. J. Emery, K. Hamilton, *J. Geophys. Res.* **90**, 857 (1985).
4. J. J. Simpson, *Geophys. Res. Lett.* **10**, 917 (1983).
5. L. L. Ely, Y. Enzel, D. R. Cayan, *J. Clim.* **7**, 977 (1994).
6. F. G. Prahl, L. A. Muehlhausen, D. L. Zahnle, *Geochim. Cosmochim. Acta* **52**, 2303 (1988).
7. P. J. Muller, G. Kirst, G. Ruhland, I. von Storch, A. Rossell-Mele, *Geochim. Cosmochim. Acta* **62**, 1757 (1998).
8. T. D. Herbert *et al.*, *Paleoceanography* **13**, 263 (1998).
9. C. L. Reimers, R. A. Jahnke, D. C. McCorkle, *Global Biogeochem. Cycles* **6**, 199 (1992).
10. N. J. Shackleton, *Science* **289**, 1897 (2000).
11. N. J. Shackleton, A. Berger, W. R. Peltier, *Trans. R. Soc. Edinburgh Earth Sci.* **81**, 251 (1990).
12. D. G. Martinson *et al.*, *Quat. Res.* **27**, 1 (1987).
13. I. J. Winograd *et al.*, *Science* **258**, 255 (1992).
14. K. R. Ludwig *et al.*, *Science* **258**, 284 (1992).
15. Alkenone and $\delta^{18}O$ data as a function of core depth and estimated age are available at ftp://pixie.geo.brown.edu.
16. G. B. Griggs, L. D. Kulm, *J. Sediment. Petrol.* **39**, 1142 (1969).
17. D. V. Kent, N. D. Opdyke, M. Ewing, *Geol. Soc. Am. Bull.* **82**, 2741 (1971).
18. P. R. Thompson, N. J. Shackleton, *Nature* **287**, 829 (1980).
19. A. L. Sabin, N. G. Pisias, *Quat. Res.* **46**, 48 (1996).
20. J. Ortiz, A. Mix, S. Hostetler, M. Kashgarian, *Paleoceanography* **12**, 191 (1997).
21. F. G. Prahl, N. Pisias, M. A. Sparrow, A. Sabin, *Paleoceanography* **10**, 763 (1995).
22. H. Doose, F. G. Prahl, M. W. Lyle, *Paleoceanography* **12**, 615 (1997).
23. J. P. Kennett, K. Venz, *Proc. ODP Sci. Res.* **146**, 281 (1995).
24. P. G. Mortyn, R. C. Thunnell, D. M. Anderson, E. Tappa, *Paleoceanography* **11**, 415 (1996).
25. E. Bard, B. Hamelin, R. G. Fairbanks, *Nature* **346**, 456 (1990).
26. J. W. Kutzbach, H. E. Wright, *Quat. Sci. Rev.* **4**, 147 (1985).
27. S. Manabe, A. J. Broccoli, *J. Geophys. Res.* **90**, 2167 (1985).
28. W. E. Dean, J. V. Gardner, D. Z. Piper, *Geochim. Cosmochim. Acta* **61**, 4507 (1997).
29. T. D. Herbert, M. Yasuda, C. Burnett, *Proc. ODP Sci. Res.* **146**, 257 (1995).
30. C. Sancetta, M. Lyle, L. Heusser, R. Zahn, J. P. Bradbury, *Quat. Res.* **38**, 359 (1992).
31. L. V. Benson *et al.*, *Palaeogogr. Palaeoclimatol. Palaeoecol.* **78**, 241 (1990).
32. W. F. Ruddiman, A. McIntyre, *Geol. Soc. Am. Bull.* **95**, 381 (1984).
33. J. Villanueva, J. O. Grimalt, E. Cortijo, L. Vidal, L. Labeyrie, *Geochim. Cosmochim. Acta* **62**, 2421 (1998).
34. T. J. Crowley, *Paleoceanography* **9**, 1 (1994).
35. R. R. Schneider *et al.*, in *The South Atlantic: Present and Past Circulation*, G. Wefer *et al.*, Eds. (Springer, New York, 1995), pp. 527–551.
36. D. W. Lea, D. K. Pak, H. J. Spero, *Science* **289**, 1719 (2000).
37. L. E. Heusser, M. Lyle, A. Mix, *Proc. ODP Sci. Res.* **167**, 217 (2000).
38. N. G. Pisias, A. C. Mix, L. Heusser, *Quat. Sci. Rev.*, in press.
39. M. Lyle, L. Heusser, T. Herbert, A. Mix, J. Barron, in preparation.
40. Sixteen pollen units were counted by L. Heusser, with the abundance of ferns tabulated as well. *Pinus* (pine) dominates the entire record, accounting for an average of 61% of the assemblage on a fern-free basis. Other significant components include *Picea* (spruce), *Tsuga heterophylla* (western hemlock), *Abies* (fir), inaperaturate conifer types (juniper/cedar), *Sequoia* (redwood), *Quercus* (oak), *Alnus* (alder), *Compositae* (sunflower family), and family *Artemesia* (sage). We extracted statistical groupings of pollen that might reflect the changes in climate. A square root transform of pollen abundance reduced the dominance of *Pinus* and produced a more Gaussian distribution of factor scores in the resultant time series than a linear transform of pollen abundance (note that one would arrive at similar pollen factors and time series results with a linear transform as well). An analysis that excluded ferns produced three factors that account for 96% of the variance in the data. Factor 1 (42% of variance explained) contains high positive loadings of *Pinus*, *Picea*, *T. heterophylla*, and *Abies*. Negative loadings of *Pinus* and family *Artemesia* characterize factor 3 (28% of variance).
41. L. E. Heusser, N. J. Shackleton, *Science* **204**, 837 (1979).
42. L. E. Heusser, *Proc. ODP Sci. Res.* **146**, 265 (1995).
43. K. L. Rosanski, Araguas-Araguas, R. Gonfiantini, in *Climate Change in Continental Isotopic Records*, P. K. Swart, K. C. Lohmann, J. McKenzie, S. Savin, Eds. (American Geophysical Union, Washington, DC, 1993), pp. 1–36.
44. R. G. Fairbanks, R. K. Matthews, *Quat. Res.* **10**, 181 (1978).
45. D. P. Schrag, G. Hampt, D. W. Murray, *Science* **272**, 1930 (1996).
46. P. M. Grootes, in *Climate Change in Continental Isotopic Records*, P. K. Swart, K. C. Lohmann, J. McKenzie, S. Savin, Eds. (American Geophysical Union, Washington, DC, 1993), pp. 37–46.
47. I. J. Winograd, T. B. Copplen, K. R. Ludwig, J. M. Landwehr, A. C. Riggs, *Eos* **77** (suppl.), S169 (1996).
48. J. Imbrie, A. C. Mix, D. G. Martinson, *Science* **363**, 531 (1993).
49. G. M. Henderson, N. C. Slowey, *Nature* **404**, 61 (2000).
50. L. D. Stott, M. Neumann, D. Hammond, *Paleoceanography* **15**, 161 (2000).
51. J. D. Schuffert, M. Kastner, R. A. Jahnke, *Mar. Geol.* **146**, 21 (1998).

52. We thank the curators of the Ocean Drilling Program and Scripps Institution of Oceanography for making samples available. Portions of this work were supported by the NSF, JOI-USSAC, the Inter-American Institute for Global Change Research, and the U.S.-Mexico Foundation for Science.

22 January 2001; accepted 25 May 2001
Published online 7 June 2001;
10.1126/science.1059290
Include this information when citing this paper.

REPORTS

Carbon Nanotube Single-Electron Transistors at Room Temperature

Henk W. Ch. Postma, Tijs Teepen, Zhen Yao,* Milena Grifoni, Cees Dekker†

Room-temperature single-electron transistors are realized within individual metallic single-wall carbon nanotube molecules. The devices feature a short (down to ~20 nanometers) nanotube section that is created by inducing local barriers into the tube with an atomic force microscope. Coulomb charging is observed at room temperature, with an addition energy of 120 millielectron volts, which substantially exceeds the thermal energy. At low temperatures, we resolve the quantum energy levels corresponding to the small island. We observe unconventional power-law dependencies in the measured transport properties for which we suggest a resonant tunneling Luttinger-liquid mechanism.

Single-electron transistors (SETs) have been proposed as a future alternative to conventional Si electronic components (*1*). However, most SETs operate at cryogenic temperatures, which strongly limits their practical application. Some examples of SETs with room-temperature operation (RTSETs) have been realized with ultrasmall grains, but their properties are extremely hard to control (*2–4*). The use of conducting molecules with well-defined dimensions and properties would be a natural solution for RTSETs. We report RTSETs made within an individual metallic carbon nanotube molecule (*5*), characterizing their transport properties as a function of temperature, bias, and gate voltage and observing unexpected power-law characteristics that we describe with a Luttinger-liquid model.

SETs consist of a conducting island connected by tunnel barriers to two metallic leads (*1*). For temperatures and bias voltages that are low relative to a characteristic energy required to add an electron to the island, electrical transport through the device is blocked. Conduction

Department of Applied Physics and DIMES, Delft University of Technology, Lorentzweg 1, 2628 CJ Delft, Netherlands.

*Present address: Department of Physics, University of Texas at Austin, Austin, TX 78712, USA.
†To whom correspondence should be addressed. E-mail: dekker@mb.tn.tudelft.nl

can be restored, however, by tuning a voltage on a close-by gate, rendering this three-terminal device a transistor. Recently, we found that strong bends ("buckles") within metallic carbon nanotubes (*5*) act as nanometer-sized tunnel barriers for electron transport (*6*). This prompted us to fabricate single-electron transistors by inducing two buckles in series within an individual metallic single-wall carbon nanotube, achieved by manipulation with an atomic force microscope (AFM) (*7*) (Fig. 1). The two buckles define a 25-nm island within the nanotube. Nanotube devices have been fabricated with an island length of between 20 and 50 nm, and electrical transport has been measured through four of them. We report one representative data set obtained on the sample with a 25-nm island.

Typical RTSET transport characteristics for our nanotube devices obtained at room temperature are shown in Fig. 2A, which displays the differential conductance dI/dV versus bias voltage V. A voltage applied to the back gate appears to have a pronounced effect on the device conductance. A 0.2-V-wide gap is observed, which is closed upon changing the gate voltage. Upon varying the gate voltage further, the gap opens and closes in a periodic manner. At $V = 0$, this gives rise to a pattern of periodic conductance peaks (Fig. 2B). It thus appears that both bias and gate voltage can be used to modulate the conductance, and a conductance spectrum where both are varied simultaneously is shown in the inset to Fig. 2B. Diamond-shaped regions are visible where the conductance is suppressed. Traces such as those in Fig. 2A are cross sections of this conductance spectrum at fixed gate voltage, whereas those in Fig. 2B are cross sections at fixed bias voltage. Before fabrication of the two buckles, the device conductance did not change with gate voltage. It is thus evident that the modulation is due to the fabricated island.

These characteristics demonstrate Coulomb blockade (i.e., single-electron tunneling) at room temperature (*1*). Coulomb blockade as a function of bias and gate voltage occurs in diamond-shaped regions (compare with the inset to Fig. 2B). Within each diamond, the number of electrons is fixed, and electrons are added one by one to the island upon increasing the gate voltage. The height of the diamonds reads the bias voltage V^+ necessary to add an electron to the island, which defines an addition energy $E_{add} = eV^+ = e^2/C + \Delta E$ (*8*), where C is the sum of all capacitances to the nanotube island and ΔE is the energy difference between consecutive quantum energy levels. We find $E_{add} = 120$ meV, which is slightly larger than the largest value of 115 meV reported in previous planar RTSETs (*4*). The Coulomb blockade model describes all the basic device characteristics shown in Fig. 2, A and B. E_{add} is much larger than the thermal energy k_BT (k_B is the Boltzmann constant and T is the absolute temperature) at room temperature, which explains the room-temperature operation of our devices.

With respect to the device characteristics at low temperature, examination of the data at 30 K (Fig. 2, C to E) reveals features that were not observed at room temperature. First, the data show less scatter owing to a reduction in sample noise at low temperatures. Second, the dI/dV (V) traces show peaked features (indicated by the lines in Fig. 2C) that shift along the bias voltage axis when changing the gate voltage. We believe that these peaks are associated with energy levels of the island that become available for electronic transport, leading to an increase in current. The peaks can be followed as a function of both bias and gate voltage in the conductance spectrum (dashed lines in Fig. 2, D and E). The distance between these lines along the bias-voltage axis is equal to $2\Delta E$. We find that $\Delta E = 38$ meV. From the linear dispersion relation of nanotubes one estimates an average $\Delta E = hv_F/4L$ for a tube of finite length L, when the degeneracy between the two sets of energy levels in nanotubes has been lifted. Here v_F is the Fermi velocity and h is Planck's constant. With $v_F = 8 \times 10^5$ m/s (*9*), we obtain 34 meV for the 25-nm island, which is in good agreement with the measured value, confirming that

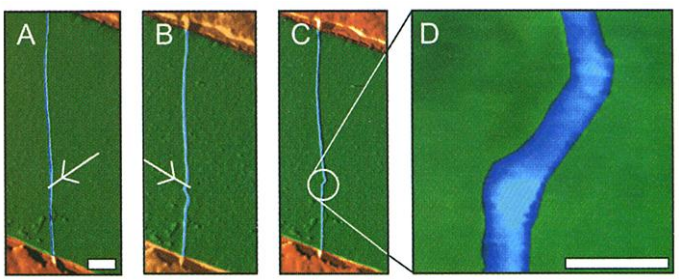

Fig. 1. Fabrication of a room-temperature single-electron transistor within an individual metallic carbon nanotube by manipulation with an AFM (*7*). (**A**) Nanotube between Au electrodes on top of a Si/SiO_2 substrate with a gate-independent resistance of 50 kilohm. After imaging by scanning the AFM tip over the sample in tapping mode, the tip is pressed down onto the substrate and moved along the path indicated by the arrow, thus dragging the nanotube into a new configuration. Bar, 200 nm. (**B**) Nanotube after creation of a buckle. The dragging action has resulted in a tube that is bent so strongly that it has buckled (*31*). A second dragging action is performed as indicated by the arrow. (**C**) Double-buckle nanotube device. (**D**) Enlarged image of the double-buckle device. The image shows a height increase at the buckling points, as expected (*31*). The final device resistance at room temperature is one order of magnitude larger (~0.5 megohm). The electronic transport properties of these nanotube devices are studied by application of a bias voltage V to the upper electrode and a measurement of the current I at the lower electrode. The differential conductance dI/dV is measured with a standard ac–lock-in technique with a modulation amplitude of 0.1 mV. The conducting Si substrate underneath the insulating SiO_2 substrate is coupled capacitively to the nanotube and acts as a back gate. Bar, 20 nm.

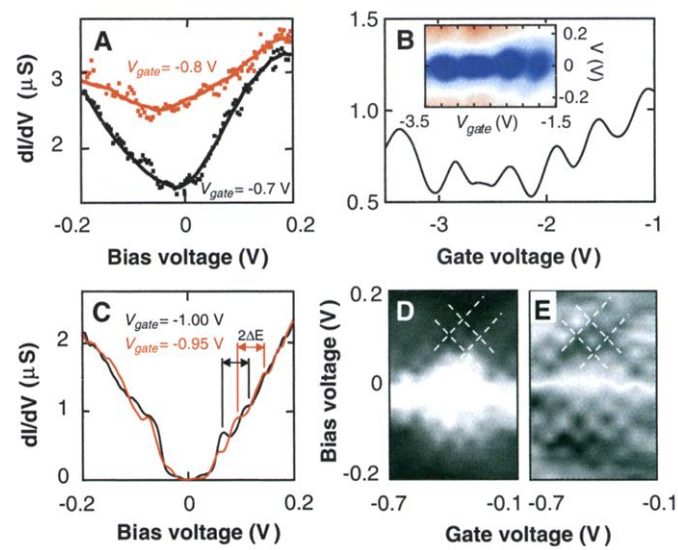

Fig. 2. Differential conductance dI/dV of the RTSET as a function of bias and gate voltage at various temperatures. (**A**) At 300 K, the differential conductance shows a thermally smeared gap around $V = 0$ with gate voltage $V_{gate} = -0.7$ V (lower trace). When the gate voltage is changed to -0.8 V, the gap is closed. (**B**) Conductance oscillations as a function of gate voltage at 260 K. (Inset) dI/dV in an intensity plot. Blue represents low dI/dV, red corresponds to high dI/dV. The gap is periodically opened and closed as a function of the gate voltage, which results in diamond-shaped modulations. (**C**) dI/dV at 30 K, showing distinct peaks as indicated by the lines. The peaks in the black trace at $V_{gate} = -1$ V shift up in bias voltage when V_{gate} is increased to -0.95 V (red trace). (**D**) Gray-scale image of dI/dV, where shifting peaks are indicated by the dashed lines. White represents $dI/dV = 0$, whereas darker shading correspond to higher values of dI/dV. (**E**) Gray-scale image of d^2I/dV^2, showing the presence of conductance peaks.

the island behaves as a well-defined quantum box for the electrons. From the addition energy we can now extract the charging energy $E_C \equiv e^2/2C$, which reads 41 meV. The fact that $\Delta E \sim E_C$ is unique to our devices, whereas in the ordinary case $E_C \gg \Delta E$. This is a direct result of the small size of these islands and the nature of the buckle junctions. In contrast to previous studies on straight undeformed nanotubes (*9–12*), the capacitances of the nanotube island to the nanotube leads (≈0.3 aF) are now a major contribution to the total capacitance C. Hence, whereas ΔE will increase with decreasing L, E_C will remain approximately constant, yielding a larger $\Delta E/E_C$ ratio.

Figure 3 shows the temperature dependence of the device conductance. A plot of a single conductance peak versus gate voltage (Fig. 3A) shows that both the conductance peak maximum G_{max} and the peak width w increase with increasing temperature. This is in marked contrast to the behavior expected for a conventional SET in both the classical ($k_BT > \Delta E$) and the quantum regime of Coulomb blockade ($k_BT < \Delta E$). In both of the latter cases $w \propto T$, but G_{max} = constant or $G_{max} \propto 1/T$, respectively (*8*). Our data also differ from previous results for carbon nanotube SET devices operating at low temperatures (*9–13*).

The conductance shows a power-law dependence on T (Fig. 4), where $G_{max}(T)$ is plotted for the peak in Fig. 3A. From 4 to 90 K, it follows a power law $G_{max} \propto T^{0.68}$, whereas at higher temperatures it increases beyond this. The inset of Fig. 4 shows that w follows a linear temperature dependence $w \propto T$ at low temperatures, whereas it deviates from the expected behavior at higher temperatures. We explain the high-temperature deviations from the overlap between adjacent peaks as follows. As the peak width increases with temperature, the peak tails start to overlap progressively with adjacent conductance peaks upon raising the temperature, leading to both a larger apparent peak height as well as a larger apparent width. We correct for this by integrating the conductance over gate voltage, yielding an integrated conductance G^*. We find a strong temperature dependence $G^* \propto T^{1.66}$, in excellent agreement with the expected behavior $G^* \propto T^{1+0.68}$ from $w(T)$ and $G_{max}(T)$. This power-law behavior persists well above the temperatures where both w and G_{max} deviate from the expected behavior, indicating that the deviations in measurements of w and G_{max} are indeed due to overlap of adjacent conductance peaks.

The power-law exponents observed in our experiments cannot be explained by the available models. Recent transport experiments on metallic carbon nanotubes (*6*, *14–16*) successfully used a Luttinger-liquid model (*17*, *18*), which derives from the one-dimensional electronic correlations in nanotubes. We therefore compare our experimental results with those from theoretical studies of a Luttinger island connected by tunnel barriers to two semi-infinite Luttinger liquids. Such studies have described transport in terms of sequential tunneling processes, with independent tunneling from the leads onto the island and from the island into the other lead (*19–22*). This leads to $G_{max} \propto T^{\alpha_{end}-1}$ and $w \propto T$, where $\alpha_{end} = \frac{1}{4}(\frac{1}{g} - 1)$, with the Luttinger interaction parameter g characterizing the electron-electron interaction strength (*17*, *18*). Experiments (*6*, *14–16*) show that g ranges between 0.19 and 0.26 in the case of carbon nanotubes, which leads to $G_{max} \propto T^{-0.2}$ and $G^* \propto T^{0.8}$, in contradiction with the present data.

We therefore propose another mechanism, namely, correlated sequential tunneling through the island. Here electrons tunnel coherently from the end of one nanotube lead to the end of the other nanotube lead through a quantum state in the island. In this picture, the island should be regarded as a single impurity (*23*). This is a reasonable assumption, because the thermal length $L_T \equiv v_F/k_BT$ = 70 nm at 300 K, and hence it is larger than the distance between the two barriers at all temperatures. The calculation for the conductance due to this tunneling mechanism yields $G_{max} \propto T^{\alpha_{end\text{-}end}-1}$ and $G^* \propto T^{\alpha_{end\text{-}end}}$, where $\alpha_{end\text{-}end} = 2\alpha_{end}$ (*24*). Upon identifying $\alpha_{end\text{-}end}$ with the experimental value 1.66, we obtain g = 0.23, in excellent agreement with earlier values for nanotubes. This shows that the proposed mechanism is the relevant transport channel for the RTSET. The surprising dominance of correlated tunneling over conventional sequential tunneling contrasts with the conventional understanding of SETs and quantum dots (*1*). Our model is further confirmed by data of the integrated differential conductance $(dI/dV)^*$ versus bias voltage at large bias ($V >$ 10 mV), which yields a power law $(dI/dV)^* \propto V^{0.87}$ (*25*). One theoretically expects that the large bias voltage $eV \gg k_BT$ will destroy the phase coherence necessary for correlated tunneling, and that conventional sequential tunneling will dominate (*24*). The expected exponent for this process is $\alpha_{end} = \alpha_{end\text{-}end}/2 = 0.83$, which is again close to the value found experimentally.

For practical applications, a figure of merit of SETs is the input equivalent charge noise q_n. Preliminary measurements on the present nanotube devices at 10 Hz and 60 K yielded $q_n \approx 2 \times 10^{-3}$ e/$\sqrt{\text{Hz}}$, which compares favorably to $q_n \approx 0.5 \times 10^{-3}$ e/$\sqrt{\text{Hz}}$ for conventional single-electron transistors that operate at mK temperatures (*26*). The prototype nanotube RTSETs presented here were obtained by manipulation with an AFM. Future use in large-scale applications will require further developments in fabrication technology such as mechanical templates or chemical methods to create short nanotubes in a parallel process. RTSETs have several advantages over room-temperature field-effect transistors using semiconducting nanotubes (*27*). Because semiconducting nanotubes are, unlike metallic tubes, intrinsically prone to disorder and unintentional doping (*28*, *29*), molec-

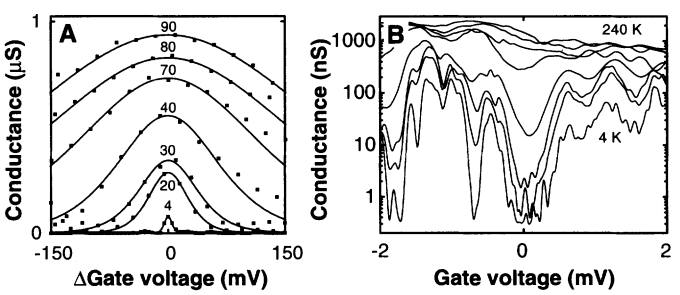

Fig. 3. (**A**) Zero-bias conductance versus gate voltage for a single conductance peak. Data are shown for T = 4, 20, 30, 40, 70, 80, and 90 K. The solid lines are fits to the function $G_{max}(T)/\cosh^2[2(\text{arccosh}\sqrt{2})V_{gate}/w(T)]$ [as derived from (*8*)]. The T dependence of the conductance maximum G_{max} and the full width at half maximum w is shown in Fig. 4. (**B**) Multiple conductance peaks on a logarithmic scale for an extended range of gate voltages at T = 4, 40, 60, 70, 100, 170, 200, 220, and 240 K.

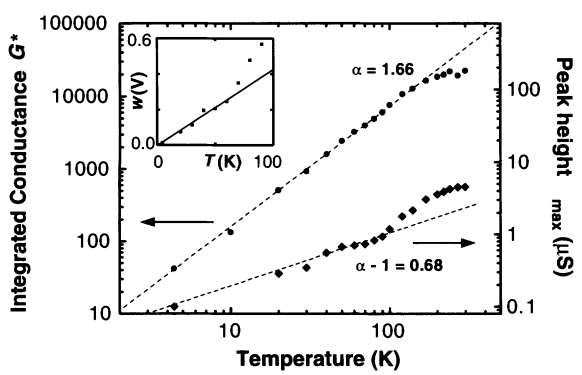

Fig. 4. Power-law temperature dependence of the conductance, demonstrating correlated sequential tunneling through the nanotube SET device. Lower data (right-hand scale) show the peak height $G_{max}(T)$ for the conductance peak in Fig. 3A, following a power-law function with exponent 0.68 (◆). The conductance integrated over the gate voltage range in Fig. 3B, $G^*(T)$ (left-hand scale), also follows a power-law function with exponent 1.66 (●). Note the double-logarithmic scales. The inset shows the peak width w versus T, which displays a linear behavior.

ular-electronics components based on metallic tubes are preferred. The present work shows that short, metallic nanotubes can be applied as RTSETs. It also serves to illustrate that the search for functional molecular devices often yields interesting fundamental science.

References and Notes

1. H. Grabert, M. Devoret, Eds., in *Single Charge Tunneling* (Plenum, New York, 1992).
2. Y. Takahashi *et al.*, *Electron. Lett.* **31**, 136 (1995).
3. K. Matsumoto *et al.*, *Appl. Phys. Lett.* **68**, 34 (1996).
4. L. Zhuang, L. Guo, S. Y. Chou, *Appl. Phys. Lett* **72**, 1205 (1998).
5. C. Dekker, *Phys. Today* **52** (5), 22 (1999).
6. H. W. Ch. Postma, M. de Jonge, Z. Yao, C. Dekker, *Phys. Rev. B* **62**, R10653 (2000).
7. H. W. Ch. Postma, A. Sellmeijer, C. Dekker, *Adv. Mater.* **17**, 1299 (2000).
8. C. W. J. Beenakker, *Phys. Rev. B* **44**, 1646 (1991).
9. S. J. Tans *et al.*, *Nature* **386**, 474 (1997).
10. M. Bockrath *et al.*, *Science* **275**, 1922 (1997).
11. D. H. Cobden, M. Bockrath, P. L. McEuen, A. G. Rinzler, R. E. Smalley, *Phys. Rev. Lett.* **81**, 681 (1998).
12. H. W. Ch. Postma, Z. Yao, C. Dekker, *J. Low Temp. Phys.* **118**, 495 (2000).
13. M. Bockrath *et al.*, *Science* **291**, 283 (2001).
14. M. Bockrath *et al.*, *Nature* **397**, 598 (1999).
15. Z. Yao, H. W. Ch. Postma, L. Balents, C. Dekker, *Nature* **402**, 273 (1999).
16. J. Nygard, D. H. Cobden, M. Bockrath, P. L. McEuen, P. E. Lindelof, *Appl. Phys. A* **69**, 297 (1999).
17. C. L. Kane, L. Balents, M. P. A. Fisher, *Phys. Rev. Lett.* **79**, 5086 (1997).
18. R. Egger, A. O. Gogolin, *Phys. Rev. Lett.* **79**, 5082 (1997).
19. C. L. Kane, M. P. A. Fisher, *Phys. Rev. Lett.* **68**, 1220 (1992).
20. A. Furusaki, *Phys. Rev. B.* **57**, 7141 (1998).
21. A. Braggio, M. Grifoni, M. Sassetti, F. Napoli, *Europhys. Lett.* **50**, 236 (2000).
22. Although the first theoretical predictions for Luttinger liquid behavior considered double-barrier devices, experimental evidence so far is scarce [see (*30*)].
23. M. P. A. Fisher, L. Balents, personal communication.
24. M. Grifoni *et al.*, unpublished data.
25. H. W. Ch. Postma, data not shown.
26. A. B. Zorin *et al.*, *Phys. Rev. B* **53**, 13682 (1996).
27. S. J. Tans, A. R. M. Verschueren, C. Dekker, *Nature* **393**, 49 (1998).
28. S. J. Tans, C. Dekker, *Nature* **404**, 834 (2000).
29. A. Bachtold *et al.*, *Phys. Rev. Lett.* **84**, 6082 (2000).
30. O. Auslaender *et al.*, *Phys. Rev. Lett.* **84**, 1764 (2000).
31. S. Iijima, C. Brabec, A. Maiti, J. Bernholc, *J. Chem. Phys.* **104**, 2089 (1996).

32. We thank R. E. Smalley and co-workers for providing the carbon nanotube material; A. Bachtold, M. P. A. Fisher, L. Balents, P. Hadley, M. Thorwart, A. Braggio, and Yu. V. Nazarov for discussions; and B. van den Enden for technical assistance. Supported by the Dutch Foundation for Fundamental Research on Matter (FOM) and the European Community SATURN project.

20 April 2001; accepted 23 May 2001

Fully Conjugated Porphyrin Tapes with Electronic Absorption Bands That Reach into Infrared

Akihiko Tsuda and Atsuhiro Osuka*

Scandium(III)-catalyzed oxidation of *meso-meso*–linked zinc(II)-porphyrin arrays (up to dodecamers) with 2,3-dichloro-5,6-dicyano-1,4-benzoquinone (DDQ) led to efficient formation of triply *meso-meso*–, β-β–, and β-β–linked zinc(II)-oligoiporphyrins with 62 to 91% yields. These fused tape-shaped porphyrin arrays display extremely red-shifted absorption bands that reflect extensively π-conjugated electronic systems and a low excitation gap. The lowest electronic absorption bands become increasingly intensified and red-shifted upon the increase in the number of porphyrins and eventually reach a peak electronic excitation for the dodecamer at ~3500 wavenumber. The one-electron oxidation potentials also decreased progressively upon the increase in the number of porphyrins. These properties in long and rigid molecular shapes suggest their potential use as molecular wires.

Discrete molecules with a very long π-system are of interest as organic conducting materials, near-infrared (near-IR) dyes, nonlinear optical materials, and molecular wires (*1–3*). Numerous attempts that have been made to extend the π-electronic systems have, however, encountered serious problems, such as synthetic inaccessibility, chemical instability, poor solubility, and conjugation saturation behavior that arises through the effective conjugated length (ECL) effect. The ECL defines the extent of π-conjugated systems in which the electronic delocalization is limited and at which point the optical, electrochemical, and other physical properties reach a saturation level that is common with the analogous polymer (*1*). A straightforward strategy for maximizing π-overlap may be to hold the π-systems coplanar within a tapelike framework by fusing the units edge-to-edge, to make a covalently linked long, flat array, but this goal is synthetically quite demanding. Fused π-conjugated systems are promising also in circumventing the above ECL limit, as seen for the [*n*]acene series (n = 1 to 7) (*1*, *4*), but extension to the higher conjugated systems suffers from problems of poor solubility caused by the resulting planar structures. Within a confined pigment number, charged dyes such as oxonols and cyanines can escape the ECL effect because of the absence of the bond alternation arising from effective resonance (*5*). Again, extension to the higher homologs is difficult to achieve and reveals the ECL effect (*6*).

Porphyrins are intriguing building units from which to construct large π-conjugated molecules. Two types of conjugated porphyrins have been developed, *meso*-ethyne–bridged and *meso*-butadiyne–bridged porphyrin arrays (*7–9*) and fused porphyrin arrays (*10–13*), both of which show unusual properties that result from strong π-conjugation. Here we report the synthesis of highly conjugated porphyrin arrays, in which the electronic π-conjugation over the arrays is far stronger than the π-conjugation of these precedents, as seen from extremely low-energy IR electronic excitations.

Recently, we reported the synthesis of *meso-meso*–linked porphyrin arrays of up to 128-oligomers by Ag^{I} salt–promoted coupling reaction (*14*). This extremely long, discrete, rodlike organic molecule has a molecular length of about 108 nm. These arrays adopt a nearly orthogonal conformation that tends to minimize the electronic interaction between the neighboring porphyrins (*14*, *15*). The aryl-end–capped *meso-meso*–linked Cu^{II}-diporphyrin **1** can be converted to triply linked fused diporphyrin **2** by the oxidative double-ring closure (ODRC) reaction upon treatment with $(p\text{-}BrC_6H_4)_3NSbCl_6$ in C_6F_6 (Scheme 1) (*13*). The planar structure of **2** has been revealed by x-ray analysis, and full conjugation over the two porphyrins has been demonstrated by its substantially broadened and red-shifted absorption spectrum.

We now describe a highly efficient synthetic method that allows the ODRC reaction of higher *meso-meso*–linked Zn(II)-porphyrins in good yields. The ODRC reaction was conducted simply by refluxing a toluene solution of *meso-meso*–linked Zn(II)-diporphyrin **3** in the presence of five equivalents of 2,3-dichloro-5,6-dicyano-1,4-benzoquinone (DDQ) and scandium trifluoromethanesulfonate [$Sc(OTf)_3$] for 0.5 hour, which afforded the triply linked fused diporphyrin **4** in 86% yield as a sole product. DDQ or $Sc(OTf)_3$ alone did not effect any change of **3**. Under similar conditions, the Zn(II)-porphyrin monomer **5** was also effectively coupled to give triply linked diporphyrin **4** in

Department of Chemistry, Graduate School of Science, Kyoto University, Sakyo-ku, Kyoto 606-8502, Japan.

*To whom correspondence should be addressed.